batteries

MDPI

Article

Synergistic Bulk and Grain-Boundary Regulation in NASICON Solid-State Electrolytes for Sodium Metal Batteries

Yifang Chen [1,†], Jingxu Wang [1,†], Jialong Chen [1], Zhuobin He [1], Caiyao Huang [1], Fengjin Qu [2,3,*] and Yajun Yue [1,*]

[1] School of Chemistry, South China Normal University, Guangzhou 510631, China; yifangchen@m.scnu.edu.cn (Y.C.); 20222421191@m.scnu.edu.cn (J.W.); 2024022652@m.scnu.edu.cn (J.C.); 2025022478@m.scnu.edu.cn (Z.H.); 2025022481@m.scnu.edu.cn (C.H.)
[2] Spallation Neutron Source Science Center, Dongguan 523803, China
[3] Institute of High Energy Physics, Chinese Academy of Sciences, Beijing 100049, China
* Correspondence: qufj@ihep.ac.cn (F.Q.); yajunyue@m.scnu.edu.cn (Y.Y.)
† These authors contributed equally to this work.

Abstract

Solid-state sodium metal batteries are promising for large-scale energy storage owing to their high safety, abundant sodium resources, and low material cost. However, NASICON-type solid-state electrolytes, such as $Na_3Zr_2Si_2PO_{12}$, still suffer from limited room-temperature ionic conductivity and poor ceramic densification. Herein, a multivalent co-doping strategy using Zn^{2+}, Sc^{3+}, Hf^{4+}, and Nb^{5+} was employed to regulate the crystal structure, sintering behavior, and Na^+ transport properties of NASICON electrolytes. The effects of isovalent and aliovalent dopants were systematically investigated by XRD, Rietveld refinement, SEM-EDS, bond-valence-site calculations, and electrochemical impedance spectroscopy. The optimized monoclinic $Na_{3.167}Zn_{0.167}Hf_{0.167}Zr_{1.5}Nb_{0.167}Si_2PO_{12}$ electrolyte delivered a room-temperature total ionic conductivity of 1.16 mS cm^{-1} and an activation energy of 0.35 eV, mainly due to optimized Na^+ migration-channel geometry and enhanced ceramic densification. Na | |Na symmetric cells exhibited stable cycling for 500 h with a maximum polarization voltage of 20 mV. Furthermore, solid-state Na | |$Na_3V_2(PO_4)_3$ cells retained 95% capacity after 624 cycles at 1 C. This work provides a feasible doping strategy for advanced NASICON electrolytes and solid-state sodium metal batteries.

Keywords: solid-state sodium batteries; NASICON; multi-element doping; solid-state electrolytes; sodium-ion transport

1. Introduction

With the rapidly increasing demand for renewable energy utilization and large-scale energy storage, developing advanced energy-storage systems with high energy density, improved safety, and low resource cost has become increasingly important [1,2]. Solid-state sodium metal batteries (SSMBs), which employ nonflammable solid-state electrolytes, offer higher safety and a wider electrochemical stability window than conventional liquid-electrolyte batteries. When coupled with sodium metal anodes, they also have the potential to deliver enhanced theoretical capacity, making them promising candidates for next-generation energy-storage technologies [3–5].

Sodium superionic conductor (NASICON)-type solid-state electrolytes possess three-dimensional Na^+ transport channels, a wide electrochemical stability window (>5.0 V), and good air stability. Among them, $Na_3Zr_2Si_2PO_{12}$ (NZSP) is one of the most representative NASICON-type sodium-ion solid-state electrolytes and has attracted considerable attention

Check for updates

Academic Editor: Yong-Joon Park

Received: 20 July 2026
Revised: 26 August 2026
Accepted: 27 August 2026
Published: 2 September 2026

Copyright: © 2026 by the authors. Licensee MDPI, Basel, Switzerland. This article is an open access article distributed under the terms and conditions of the Creative Commons Attribution (CC BY) license.

for solid-state sodium metal batteries [5–7]. In 1976, Goodenough et al. first reported the fast Na^+ transport capability of NZSP [8]. Since then, extensive studies have been conducted on the crystal structure, electrochemical properties, and battery applications of NZSP-based electrolytes [9–13]. The crystal framework of NZSP is composed of ZrO_6 octahedra and SiO_4/PO_4 tetrahedra connected through corner-sharing oxygen atoms, while Na^+ ions occupy the interstitial sites between these polyhedral units, forming a fast ion-conduction network. Pristine NZSP typically exhibits relatively low room-temperature ionic conductivity, approximately 10^{-4} S cm^{-1}, which is lower than that of halide and sulfide solid-state electrolytes [14,15]. Nevertheless, NZSP remains highly attractive because of its good air and chemical stability as well as its relatively mature ceramic-processing route.

In general, isovalent or aliovalent substitution at the Zr site can effectively regulate the ZrO_6–SiO_4/PO_4 framework, enlarge the Na^+ transport bottleneck, and thereby improve ionic conductivity. Low-valence dopants can also increase the concentration of mobile charge carriers, further enhancing Na^+ conduction. Previous studies have shown that NZSP-based electrolytes usually exhibit favorable ionic transport when the Na^+ content is in the range of 3.0–3.3 [8,9]. Depending on the type and amount of dopants, NZSP can crystallize at room temperature in either a monoclinic phase with the $C2/c$ space group or a rhombohedral phase with the $R\bar{3}c$ space group. For example, previous reports have shown that Zn-doped or Cu-doped monoclinic NZSP electrolytes can achieve room-temperature ionic conductivities on the order of 10^{-3} S cm^{-1} [16–20]. Rhombohedral NZSP-based electrolytes with high ionic conductivity have also been reported [21]. Although there is still no consensus on whether the monoclinic or rhombohedral phase is intrinsically more favorable for Na^+ transport, it is generally accepted that widening the Na^+ migration channels is beneficial for improving ionic conductivity in both phases.

In addition to intrinsic ionic transport, NZSP ceramics also face challenges associated with insufficient densification during solid-state sintering. Residual pores between ceramic grains can interrupt continuous Na^+ transport pathways and thus limit the overall ionic conductivity. Meanwhile, the porous ceramic structure reduces the mechanical strength of the solid electrolyte, which facilitates the growth of sodium dendrites along grain boundaries and increases the risk of short circuits. Grain-boundary engineering and bulk doping are two common strategies for improving the comprehensive performance of NZSP electrolytes. For example, the introduction of a CuO–B_2O_3 liquid-phase sintering aid can promote grain-boundary densification, enabling the optimized NZSP-0.2CBO to achieve an ionic conductivity of 0.64 mS cm^{-1}, with the symmetric cell exhibiting stable cycling for 850 h at 0.1 mA cm^{-2} [22]. In addition, elemental doping can also effectively improve the sintering density and grain-boundary transport properties of NZSP ceramics. For instance, Sc^{3+}/Zn^{2+} co-doping widens the Na^+ migration channel and promotes electrolyte densification, allowing the optimized NZSP to deliver an ionic conductivity of 2.41 mS cm^{-1} and a low activation energy of 0.20 eV [23]. For the moment, the synergistic modification of both the bulk structure and grain-boundary properties by elemental doping remains insufficiently understood.

Based on these considerations, this work proposes a multi-element co-doping strategy by introducing different cations (Zn^{2+}, Sc^{3+}, Hf^{4+} and Nb^{5+}) into the Zr^{4+} site of NZSP. The doped cations with different ionic radii and valence states can tune the carrier concentration, lattice parameters, and migration-channel bottleneck size, thereby improving Na^+ transport kinetics. In addition, dopant precursors such as ZnO may act as sintering aids during high-temperature ceramic processing, leading to improved ceramic densification. To clarify the synergistic effect of multi-element doping, two doped NZSP systems were designed in this work: $Na_{3.167}Zn_{0.167}Hf_xZr_{1.667-x}Nb_{0.167}Si_2PO_{12}$ ($0 \leq x \leq 0.667$), in which the isovalent dopant (Hf^{4+}) was varied to regulate the pathway;

and $Na_{3.333}Zn_{0.167}Sc_{0.167}Hf_xZr_{1.5-x}Nb_{0.167}Si_2PO_{12}$ ($0 \leq x \leq 0.667$), in which a low-valence dopant (Sc^{3+}) was further incorporated to increase the Na^+ concentration and to examine the influence of Na^+ stoichiometry on ionic conductivity. Through room-temperature ionic-conductivity screening, the optimized composition $Na_{3.167}Zn_{0.167}Hf_{0.167}Zr_{1.5}Nb_{0.167}Si_2PO_{12}$ was identified. Its phase structure, Na^+ transport channels, sintering density, and elemental distribution were systematically investigated by X-ray diffraction, Rietveld refinement, bond-valence-site calculations, and SEM-EDS analysis. Finally, the electrochemical performance of the optimized electrolyte was further validated in solid-state sodium metal batteries. This study provides useful insight into multi-element co-doping strategies for NASICON-type solid-state electrolytes and offers guidance for the development of advanced solid-state sodium batteries.

2. Materials and Methods

2.1. Preparation of NASICON Solid-State Electrolytes

NASICON solid-state electrolytes were prepared by a solid-state reaction. Stoichiometric amounts of Na_2CO_3 (Aladdin, Shanghai, China), $NH_4H_2PO_4$ (Aladdin, Shanghai, China), ZrO_2 (Innochem, Beijing, China), SiO_2 (Aladdin, Shanghai, China), ZnO (Aladdin, Shanghai, China), Sc_2O_3 (Aladdin, Shanghai, China), HfO_2 (Aladdin, Shanghai, China), and Nb_2O_5 (Macklin, Shanghai, China) were mixed using ethanol as a dispersion reagent and ball-milled at 300 rpm for 12 h. The resulting slurry was dried at 80 °C and then calcined in air at 800 °C for 12 h with a heating rate of 5 °C min^{-1} to obtain the pre-sintered precursor. The product was thoroughly ground and ball-milled at 300 rpm for 12 h. The obtained powder was pressed into green pellets with a diameter of approximately 15 mm and a thickness of approximately 1 mm under a pressure of 200 MPa for 5 min. Finally, the green pellets were sintered in a muffle furnace at 1050 °C for 12 h with a heating rate of 5 °C min^{-1} to obtain dense NASICON solid-state electrolyte pellets. The samples were named according to the type and content of the dopant elements, as summarized in Table 1.

Table 1. Sample names and corresponding dopant types and contents.

	Chemical Formula	Hf Content	Abbreviations
System 1	$Na_3Zr_2Si_2PO_{12}$	0	NZSP
	$Na_{3.167}Zn_{0.167}Zr_{1.667}Nb_{0.167}Si_2PO_{12}$	0	NZSP-1
	$Na_{3.167}Zn_{0.167}Hf_{0.167}Zr_{1.5}Nb_{0.167}Si_2PO_{12}$	0.167	NZSP-2
	$Na_{3.167}Zn_{0.167}Hf_{0.333}Zr_{1.333}Nb_{0.167}Si_2PO_{12}$	0.333	NZSP-3
	$Na_{3.167}Zn_{0.167}Hf_{0.667}Zr_1Nb_{0.167}Si_2PO_{12}$	0.667	NZSP-4
System 2	$Na_{3.333}Zn_{0.167}Sc_{0.167}Zr_{1.5}Nb_{0.167}Si_2PO_{12}$	0	NZSP-Sc1
	$Na_{3.333}Zn_{0.167}Sc_{0.167}Hf_{0.167}Zr_{1.333}Nb_{0.167}Si_2PO_{12}$	0.167	NZSP-Sc2
	$Na_{3.333}Zn_{0.167}Sc_{0.167}Hf_{0.333}Zr_{1.167}Nb_{0.167}Si_2PO_{12}$	0.333	NZSP-Sc3
	$Na_{3.333}Zn_{0.167}Sc_{0.167}Hf_{0.667}Zr_{0.833}Nb_{0.167}Si_2PO_{12}$	0.667	NZSP-Sc4

2.2. Electrochemical Impedance Spectroscopy

The ionic conductivity was determined by electrochemical impedance spectroscopy (EIS) on a electrochemical working station (VMP-3, Bio-Logic SAS, France). Before testing, the sintered pellets were polished to a size with a diameter of ca. 14.0 mm and a thickness of 0.95 mm and then coated with Au as ion-blocking electrodes. EIS measurements were conducted using a Bio-Logic VMP3 electrochemical workstation under the bias of 10 mV over a frequency range of 1 MHz to 0.1 Hz at ambient pressure. The obtained impedance spectra were fitted using equivalent circuits to distinguish the bulk resistance (R_b), grain-boundary resistance (R_{gb}), and total resistance (R_t). The Au||Au cell was measured

using direct current (DC) polarization (1 V) to evaluate the electronic conductivity of the electrolyte.

The ionic conductivity was calculated according to the following equation:

$$\sigma = L/(RS)$$

where L is the thickness of the electrolyte pellet, R is the fitted resistance, and S is the effective electrode area. To evaluate the effect of multi-element doping on Na^+ migration kinetics, temperature-dependent EIS measurements were performed on representative samples. The activation energy for Na^+ transport was calculated according to the Arrhenius relationship:

$$\sigma = A \exp(-E_a/k_B T)$$

where σ is the ionic conductivity, T is the absolute temperature, A is the pre-exponential factor, E_a is the activation energy for Na^+ transport, and k_B is the Boltzmann constant.

2.3. Structural and Morphological Characterization

Powder X-ray diffraction (XRD) patterns were collected using a Bruker D8 Advance X-ray diffractometer (Germany) with Cu Kα radiation. The diffraction data were recorded over a 2θ range of 5–90° at a scanning rate of 1.8° min^{-1}. The obtained XRD patterns were further analyzed by Rietveld refinement using a monoclinic $C2/c$ structural model with initial lattice parameters of a = 15.645 Å, b = 9.047 Å, c = 9.180 Å, and β = 123.681° [24].

The microstructure and elemental distribution of the samples were characterized by field-emission scanning electron microscopy (GeminiSEM 500, ZEISS, Germany) equipped with energy-dispersive X-ray spectroscopy (EDS). To observe the internal morphology of the ceramic pellets, the electrolyte pellets were fractured longitudinally before characterization, and the fracture surfaces were examined. Because NASICON ceramics have low electronic conductivity, the fracture surfaces were sputter-coated with Pt–Au before SEM observation.

2.4. Solid-State Cell Assembly and Electrochemical Testing

Na | | Na symmetric cells were assembled using two sodium metal disks with the same size. Sodium metal was cut into circular disks and attached to both sides of the NASICON electrolyte pellet to assemble coin cells. All cell-assembly procedures were carried out in an Ar-filled glovebox, where the H_2O and O_2 contents were both maintained below 0.1 ppm. Galvanostatic cycling was performed at room temperature to evaluate the compatibility between the solid-state electrolyte and sodium metal. The cells were cycled at a current density of 0.1 mA cm^{-2} with an areal capacity of 0.1 mAh cm^{-2}, and the polarization voltage was recorded as a function of cycling time.

For the Na | NASICON | $Na_3V_2(PO_4)_3$ cells, $Na_3V_2(PO_4)_3$ (NVP) cathode active material, with a theoretical capacity of 117 mAh g^{-1}, conductive carbon black, and poly(vinylidene fluoride) (PVDF) were mixed at a mass ratio of 7:2:1. An appropriate amount of N-methyl-2-pyrrolidone (NMP) was then added to form a homogeneous slurry. The slurry was coated onto Al foil, dried at 65 °C for 2 h, and further vacuum-dried at 100 °C for 13 h. The loading mass of the cathode active material was controlled at 1–1.5 mg cm^{-2}.

Sodium metal was used as the anode, and the NASICON ceramic pellet was used as the solid-state electrolyte. Na | NASICON | NVP coin cells were assembled in an Ar-filled glovebox. Specifically, a sodium metal disk was attached to one side of the solid-state electrolyte, while the NVP cathode was placed on the other side. To improve the interfacial wettability between the cathode and the solid-state electrolyte, 10 μL of 1 M $NaPF_6$ in diglyme was added to the cathode side. The assembled cells were tested on a LAND battery-testing system (CT2001A, LAND, China) by galvanostatic charge–discharge

measurements within a voltage range of 2.2–3.8 V. The electrochemical performance of the cells was evaluated by rate-capability tests and long-term cycling tests at 1 C.

3. Results and Discussion

3.1. Rational Design of the Chemical Composition of NASICON Solid-State Electrolytes

The Na^+ transport behavior in NZSP is closely associated with elemental substitution at the Zr site. On the one hand, doping an element with lower valence can increase the concentration of mobile charge carriers. On the other hand, it can enlarge the bottleneck size of Na^+ migration channels and reduce the ion-migration energy barrier. According to the ionic conductivity relationship for solid-state ion conductors:

$$\sigma = \Sigma n_i e_i \mu_i$$

where n_i is the concentration of charge carrier i, e_i is the ionic charge, and μ_i is the ionic mobility; increasing both the carrier concentration and the ion mobility is beneficial for improving ionic conductivity.

In the current work, a multi-element co-doping strategy was adopted to regulate the Na^+ transport behavior in $Na_3Zr_2Si_2PO_{12}$. First, low-valence dopants were partially introduced at the Zr site to increase the Na^+ concentration. Second, Zn^{2+} and Sc^{3+}, which possess slightly larger ionic radii than Zr^{4+}, were incorporated to enlarge the Na^+ transport channels. Third, Hf^{4+} and Nb^{5+} were introduced to balance local lattice distortion and improve the structural stability of the doped NASICON framework. In addition, previous studies have suggested that Zn incorporation can facilitate grain-boundary fusion in NASICON ceramics, thereby improving the densification of ceramic electrolytes [23].

Based on this design concept, two multi-element-doped systems were investigated in this work: $Na_{3.167}Zn_{0.167}Hf_xZr_{1.667-x}Nb_{0.167}Si_2PO_{12}$ (system 1) and $Na_{3.333}Zn_{0.167}Sc_{0.167}Hf_xZr_{1.5-x}Nb_{0.167}Si_2PO_{12}$ (system 2). The former was designed to study the influence of isovalent Hf/Zr substitution on electrochemical behavior by varying the Hf/Zr ratio. The latter contains the low-valence dopant Sc^{3+} and therefore has a higher Na^+ content, allowing the influence of Na^+ stoichiometry on the bulk, grain-boundary, and total ionic conductivities to be examined. The design principle is schematically illustrated in Figure 1. Considering the similar ionic radii and chemical properties of Hf^{4+} and Zr^{4+}, varying the Hf/Zr ratio is expected to minimize the influence of lattice-size mismatch while allowing the role of multi-element composition on ionic transport and grain-boundary behavior to be evaluated. This design helps clarify how elemental doping regulates the structure and electrochemical properties of NASICON electrolytes.

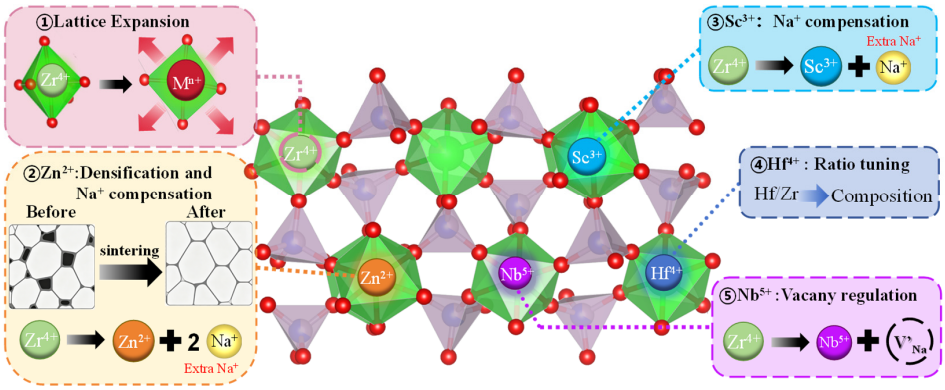


Figure 1. Schematic illustration of the NASICON solid-state electrolyte structure and the proposed elemental-doping strategy for regulating Na^+ transport. Note the tetrahedra represent Si/PO_4 and the red sphere represents oxygen atom.

3.2. Electrochemical Properties of NASICON Solid-State Electrolytes

Room-temperature electrochemical impedance spectroscopy (EIS) measurements show that the Nyquist plots of all samples consist of a semicircle in the high-frequency region and an inclined line in the low-frequency region (Figure S1). The left intercept of the semicircle with the *x*-axis is assigned to the bulk resistance, R_b, while the diameter of the semicircle mainly corresponds to the grain-boundary resistance, R_{gb}. The inclined line in the low-frequency region originates from ion polarization at the blocking-electrode interface. The Nyquist plots of the NZSP samples were fitted using the equivalent circuit shown in Figure S2a, and a representative fitting result is presented in Figure S2b. The fitted resistance values, including R_b and R_{gb}, together with the corresponding bulk conductivity, σ_b, and total ionic conductivity, σ_t, are summarized in Table 2 and Figure 2a,b.

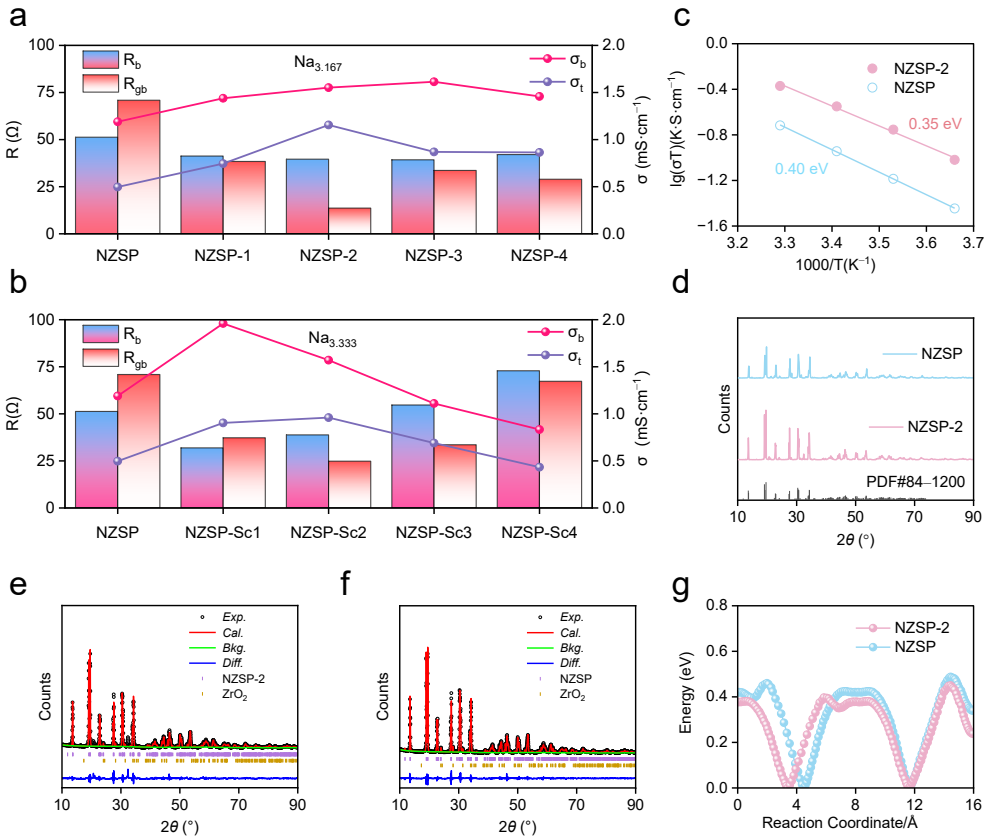


Figure 2. Electrochemical and structural characterization of NASICON solid-state electrolytes. Ionic conductivities and resistance values of samples in (**a**) system 1 and (**b**) system 2. (**c**) Arrhenius plots of NZSP-2 and pristine NZSP. (**d**) XRD patterns of pristine NZSP and NZSP-2. Rietveld refinement profiles of (**e**) NZSP-2 and (**f**) pristine NZSP. (**g**) Na^+ migration energy barriers calculated by the BVSE method.

For system 1, namely $Na_{3.167}Zn_{0.167}Hf_xZr_{1.667-x}Nb_{0.167}Si_2PO_{12}$, both σ_b and σ_t are higher than those of the pristine NZSP. With increasing Hf content, both values first increase and then decrease. It should be noted that σ_t is affected by both bulk and grain-boundary contributions, making its variation more complex. Since elemental doping directly modifies the internal structure of ceramic grains, the following discussion focuses mainly on the variation in σ_b. At a relatively lower Na content ($Na_{3.167}$), the structure has a high concentration of Na-site vacancy, which means the vacancy-assisted Na^+ transport has optional directions. Although the Hf^{4+} (0.71 Å) has a slightly smaller ionic radius than Zr^{4+} (0.72 Å) [25], which may lead to a smaller bottleneck nearby, the abundance of pathways still enables relatively high Na^+ conduction capability. This is reflected by the experimental σ_b values for *x* in-

creasing from 0 to 0.333 in system 1 (i.e., the red line shown in Figure 2a). Introducing lower-valence Sc^{3+} into the structure, as in system 2, significantly enhances σ_b. For example, the σ_b increases from 1.55 mS cm^{-1} for $Na_{3.167}Zn_{0.167}Hf_{0.167}Zr_{1.5}Nb_{0.167}Si_2PO_{12}$ (NZSP-2 in system 1) to 1.96 mS cm^{-1} for $Na_{3.333}Zn_{0.167}Sc_{0.167}Hf_{0.167}Zr_{1.333}Nb_{0.167}Si_2PO_{12}$ (NZSP-Sc2 in system 2), which can be attributed to the increased carrier concentration caused by the higher Na^+ content, from 3.167 to 3.333. Interestingly, when Hf is further introduced, the bulk conductivity of system 2 decreases rapidly. This may be because, at a higher Na content ($Na_{3.333}$), the reduced concentration of Na vacancies has limited the availability of neighboring hopping sites; therefore, excessive Hf substitution with contraction of the transport bottleneck eventually deteriorates the bulk conductivity. These results indicate that the mobility of charge carriers in solid-state ion conductors is strongly governed by their local chemical environment.

Table 2. Bulk and total ionic conductivities of different samples obtained from electrochemical impedance spectroscopy fitting.

Order	Chemical Formula	Bulk (mS cm^{-1})	Total (mS cm^{-1})
1	$Na_3Zr_2Si_2PO_{12}$	0.83	0.43
2	$Na_{3.167}Zn_{0.167}Zr_{1.667}Nb_{0.167}Si_2PO_{12}$	1.44	0.75
3	$Na_{3.167}Zn_{0.167}Hf_{0.167}Zr_{1.5}Nb_{0.167}Si_2PO_{12}$	1.55	1.16
4	$Na_{3.167}Zn_{0.167}Hf_{0.333}Zr_{1.333}Nb_{0.167}Si_2PO_{12}$	1.61	0.87
5	$Na_{3.167}Zn_{0.167}Hf_{0.667}Zr_1Nb_{0.167}Si_2PO_{12}$	1.46	0.86
6	$Na_{3.333}Zn_{0.167}Sc_{0.167}Zr_{1.5}Nb_{0.167}Si_2PO_{12}$	1.19	0.50
7	$Na_{3.333}Zn_{0.167}Sc_{0.167}Hf_{0.167}Zr_{1.333}Nb_{0.167}Si_2PO_{12}$	1.96	0.90
8	$Na_{3.333}Zn_{0.167}Sc_{0.167}Hf_{0.333}Zr_{1.167}Nb_{0.167}Si_2PO_{12}$	1.57	0.96
9	$Na_{3.333}Zn_{0.167}Sc_{0.167}Hf_{0.667}Zr_{0.833}Nb_{0.167}Si_2PO_{12}$	0.83	0.43

For all samples in the two systems, the total ionic conductivity σ_t is lower than the corresponding bulk conductivity σ_b because of the contribution from grain-boundary resistance. For $Na_{3.167}Zn_{0.167}Hf_{0.167}Zr_{1.5}Nb_{0.167}Si_2PO_{12}$ (NZSP-2 in system 1), with x = 0.167, although its σ_b is not the highest among all samples, reaching 1.55 mS cm^{-1}, it exhibits the highest σ_t of 1.16 mS cm^{-1}, which is significantly higher than those of the other compositions in this series. This result suggests that the bulk and grain-boundary conductivities are optimally balanced in this composition; therefore, NZSP-2 is identified as the optimized composition. The R_b and R_{gb} values of different samples further indicate that an appropriate amount of Hf^{4+} substitution can reduce the grain-boundary resistance, compared with the pristine NZSP, possibly by improving grain contact or suppressing the formation of grain-boundary defects during sintering. The Arrhenius plots (Figure 2c) show that NZSP-2 exhibits higher ionic conductivity than pristine NZSP over the measured temperature range, along with a lower activation energy of 0.35 eV compared with 0.40 eV for NZSP. In addition, the DC polarization measurement results (Figure S3) suggest that NZSP-2 and NZSP have comparable electronic conductivity of 3.28×10^{-8} S cm^{-1} and 3.43×10^{-8} S cm^{-1} respectively.

3.3. Structue and Morphology

The XRD patterns show that the diffraction peaks of the optimized composition $Na_{3.167}Zn_{0.167}Hf_{0.167}Zr_{1.5}Nb_{0.167}Si_2PO_{12}$, denoted as NZSP-2, and pristine NZSP are consistent with those of monoclinic NASICON, according to PDF#84-1200 (Figure 2d). Rietveld refinement was performed using a monoclinic $C2/c$ structural model, and the fitting results are shown in Figure 2e,f. The corresponding refinement parameters and refined atomic parameters are listed in Tables A1 and A2, with selected critical bond lengths listed in

Tables A3 and A4. Two tiny impurity peaks appear in the pattern of NZSP-2, while its phase cannot be identified.

Compared with pristine NZSP, NZSP-2 shows slight increases in the lattice parameters *a* and *c*. The unit-cell volume increases from 1084 $Å^3$ to 1085 $Å^3$, mainly due to the incorporation of larger Zn^{2+} ions. In the monoclinic structure, three crystallographically inequivalent Na^+ sites are present. Among them, the Na3 site is formed by the splitting of the Na2 site in the rhombohedral phase during the phase transition to the monoclinic structure [8]. It is generally accepted that Na1 represents a relatively low-energy and stable occupation site, whereas Na2 is a relatively high-energy site [26]. Therefore, Na3, derived from the splitting of Na2, can also be regarded as a high-energy site. Based on the above site energy differences and structural relationships, the Na2–Na1–Na3 pathway was selected as the potential Na^+ migration pathway. Along this pathway, migrating Na^+ ions need to pass through several bottlenecks (Figure S4). Specifically, Na^+ migration between the Na2–Na1 and Na1–Na3 sites occurs through the S1/S2 and S3/S4 bottleneck triangles, respectively. The refined structural model shows that the Na3–Na1 bottleneck area in NZSP-2 is similar to that in pristine NZSP, whereas the Na2–Na1-related bottleneck areas increase from 6.21/5.16 $Å^2$ in NZSP to 6.42/5.35 $Å^2$ in NZSP-2. This indicates that elemental doping effectively enlarges the Na^+ migration bottleneck.

Bond-valence-site energy (BVSE) calculations [27] were further performed to evaluate the theoretical Na^+ migration pathways (Figure S5) and migration barriers (Figure 2g). The results show that NZSP-2 generally possesses lower Na^+ migration barriers than pristine NZSP, suggesting that multi-element doping improves Na^+ migration kinetics in NASICON. The maximum migration barrier calculated by BVSE decreases from 0.49 eV to 0.45 eV, which is consistent with the decrease in activation energy obtained from the Arrhenius plots from 0.40 eV to 0.35 eV.

Cross-sectional SEM images of NZSP-2 and pristine NZSP are shown in Figure 3a and Figure S6, respectively. The sintered NZSP sample contains many pores between grains, and the grains are poorly fused, indicating a relatively low degree of densification. In contrast, the optimized doped sample exhibits more uniform and compact grain fusion, forming a continuous ceramic matrix. This suggests that elemental doping improves the sintering densification and grain-boundary bonding of NASICON ceramics. Such microstructural improvement is beneficial for enhancing ion conduction across grain boundaries and reducing the risk of sodium metal penetration along pores or grain boundaries.

EDS mapping shows that Na, Zr, Si, P, and O are uniformly distributed in pristine NZSP, consistent with its single NASICON main phase (Figure S7). For NZSP-2, in addition to Na, Zr, Si and P, the doped Zn, Nb and Hf elements are also uniformly distributed throughout the examined region (Figure 3b–i). Notably, Zn shows local enrichment near grain boundaries. Based on the Rietveld refinement results and the increased lattice parameters, Zn is considered to be partially incorporated into the NASICON lattice. Previous studies have also shown that Zn-containing species can act as sintering aids and promote intergrain fusion. These results collectively indicate that multi-element doping not only maintains the stable NASICON main phase and broadens the Na^+ migration channels, but also improves ceramic densification during sintering. The densification percentages of NZSP, NZSP-1, NZSP-2, and NZSP-4 were further calculated as 87.72%, 89.95%, 92.28% and 90.12%, respectively, by using a mass-to-volume method, which also proves the strengthened densification with Zn doping. Overall, the combined effects of crystal-structure regulation, improved ceramic densification, and optimized Na^+ migration pathways contribute to the enhanced room-temperature ionic conductivity of the optimized composition.

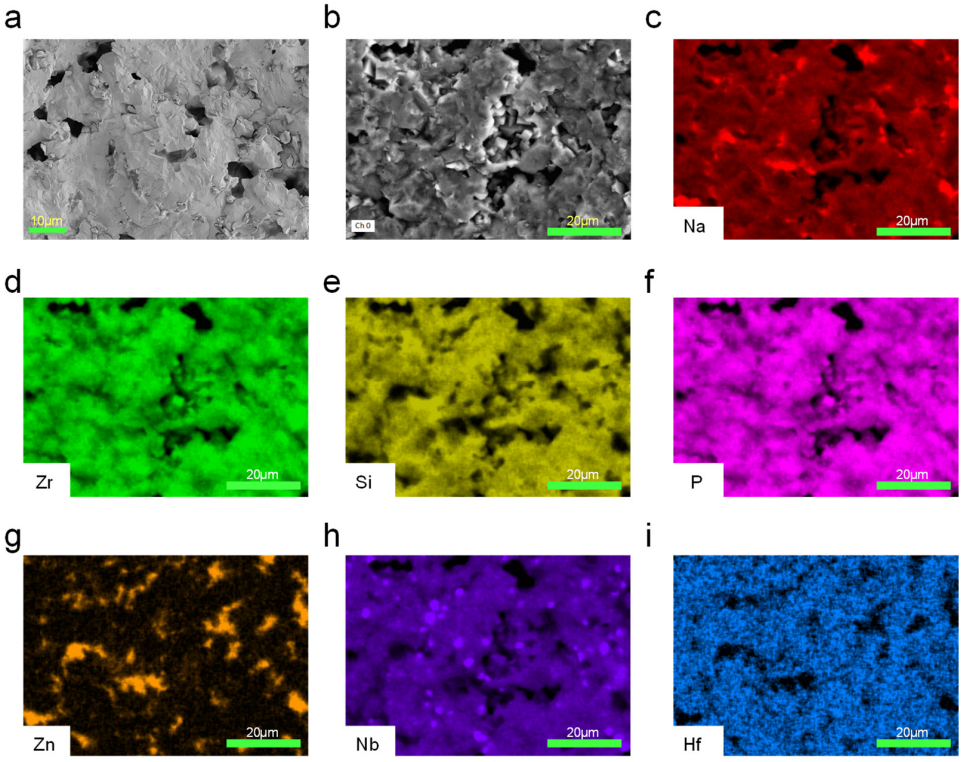


Figure 3. Morphological and elemental-distribution characterization of the optimized sample. (**a**) Cross-sectional SEM image of the optimized NASICON electrolyte. (**b**) Selected SEM image and corresponding (**c**–**i**) EDS elemental mapping results for Na, Zr, Si, P, Zn, Nb, and Hf.

3.4. Performance Evaluation of Solid-State Sodium Metal Batteries

To evaluate the practical applicability of the multi-element-doped NASICON solid-state electrolyte in solid-state battery devices, a Na | $Na_{3.167}Zn_{0.167}Hf_{0.167}Zr_{1.5}Nb_{0.167}Si_2PO_{12}$ | Na symmetric cell was first assembled using NZSP-2. This cell was used to assess the stability of sodium plating/stripping and the interfacial compatibility between the electrolyte and the sodium metal anode. As shown in Figure 4a, the symmetric cell exhibited stable cycling for more than 500 h at room temperature under a current density of 0.1 mA cm^{-2}. The initial polarization voltage was approximately 11 mV and only gradually increased to approximately 19 mV after 500 h. No sudden voltage drop associated with short circuiting was observed, indicating good interfacial compatibility and electrochemical stability between the optimized electrolyte and sodium metal. Such stable cycling is consistent with previous studies highlighting the importance of intimate solid–solid contact and stable interphase for plating/stripping [28–32]. This behavior can be attributed to the improved ceramic densification of the optimized electrolyte and high room-temperature ionic conductivity, which reduces polarization and enhances cell stability. The dendrite-free behavior was also supported by the cross-section SEM image of the NZSP-2 electrolyte after cycling, as shown in Figure S8.

Na | $Na_{3.167}Zn_{0.167}Hf_{0.167}Zr_{1.5}Nb_{0.167}Si_2PO_{12}$ | $Na_3V_2(PO_4)_3$ solid-state sodium metal full cells were further assembled using $Na_3V_2(PO_4)_3$ (NVP) as the cathode to evaluate the rate capability and long-term cycling stability. As shown in Figure 4b, the cell maintained high reversible capacities over a wide rate range from 0.1 C to 5 C, delivering specific capacities of 108.6, 102.7, and 97.7 mAh g^{-1} at 0.1 C, 1 C, and 5 C, respectively. When the rate was returned to 1 C, the capacity recovered to 102.2 mAh g^{-1}, demonstrating good electrochemical reversibility. At room temperature and 1 C, the full cell retained 95% of its capacity after 624 cycles and remained stable for more than 700 cycles. The corresponding charge–discharge profiles further confirm the high cycling stability of the cell (Figure 4d).

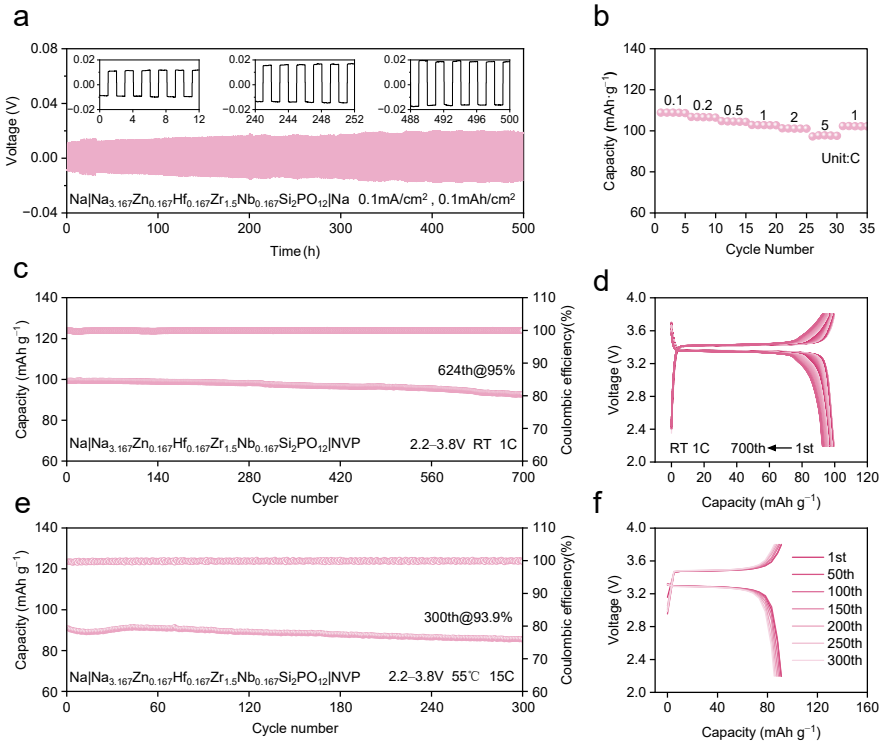


Figure 4. Electrochemical performance of solid-state sodium metal cells based on the optimized NASICON electrolyte. (**a**) Galvanostatic cycling performance of the Na | $Na_{3.167}Zn_{0.167}Hf_{0.167}Zr_{1.5}Nb_{0.167}Si_2PO_{12}$ | Na symmetric cell at room temperature under 0.1 mA cm^{-2} and 0.1 mAh cm^{-2}. (**b**) Rate capability of the Na | $Na_{3.167}Zn_{0.167}Hf_{0.167}Zr_{1.5}Nb_{0.167}Si_2PO_{12}$ | NVP cell at room temperature. (**c**) Long-term cycling performance of the Na | $Na_{3.167}Zn_{0.167}Hf_{0.167}Zr_{1.5}Nb_{0.167}Si_2PO_{12}$ | NVP cell at 1 C and room temperature. (**d**) Charge–discharge profiles during cycling at 1 C and room temperature. (**e**) Long-term cycling performance of the Na | $Na_{3.167}Zn_{0.167}Hf_{0.167}Zr_{1.5}Nb_{0.167}Si_2PO_{12}$ | NVP cell at 15 C and 55 °C. (**f**) Representative charge–discharge profiles during cycling at 15 C and 55 °C.

Based on this promising battery performance, long-term cycling tests of the Na | | NVP full cell were further conducted at an elevated temperature and high rate. Even at 55 °C and 15 C, the cell maintained stable cycling for 300 cycles with a high capacity retention of 93.9% (Figure 4e,f). These results demonstrate that the multi-element-doped NASICON electrolyte not only exhibits high room-temperature ionic conductivity and low Na^+ migration activation energy, but also enables stable long-term operation of solid-state sodium batteries.

4. Conclusions

In this work, a series of NASICON-type inorganic solid-state electrolytes based on $Na_3Zr_2Si_2PO_{12}$ were designed and synthesized through a multi-element co-doping strategy. By comparing the ionic transport properties of samples with different Na^+ concentrations and Hf^{4+}/Zr^{4+} substitution ratios, $Na_{3.167}Zn_{0.167}Hf_{0.167}Zr_{1.5}Nb_{0.167}Si_2PO_{12}$ was identified as the optimized composition. This composition retains the monoclinic NASICON structure and exhibits slightly enlarged lattice parameters and unit-cell volume, providing wider Na^+ transport channels. In addition, cross-sectional morphology observations reveal closer grain contact and improved ceramic densification, which are beneficial for reducing grain-boundary resistance to Na^+ transport.

Owing to the combined advantages of crystal-structure regulation and grain-boundary optimization, the optimized electrolyte delivers a room-temperature total conductivity of 1.16 mS cm^{-1}, significantly higher than that of pristine $Na_3Zr_2Si_2PO_{12}$, which exhibits 0.43 mS cm^{-1}. Temperature-dependent impedance analysis further shows that the Na^+

transport activation energy decreases to 0.35 eV. Na||Na symmetric cells assembled with the optimized electrolyte can cycle stably for more than 500 h, with a final polarization voltage of only 19 mV, indicating favorable interfacial stability with sodium metal. Furthermore, Na||NVP solid-state sodium cells retain 95% of their capacity after 624 cycles at 1 C and 93.9% after 300 cycles at 15 C, demonstrating excellent long-term cycling stability. This study provides a feasible strategy for the compositional design of advanced NASICON-type oxide solid-state electrolytes and offers guidance for the development of high-performance solid-state sodium metal batteries.

Supplementary Materials: The following supporting information can be downloaded at https://www.mdpi.com/article/10.3390/batteries12090334/s1, Figure S1: AC impedance spectra of the samples: (a) System 1 and (b) the corresponding high-frequency enlarged view; (c) System 2 and (d) the corresponding high-frequency enlarged view; Figure S2: (a) Equivalent circuit model and (b) fitting result of the AC impedance data for NZSP; Figure S3: Direct current polarization measurement results for (a) NZSP-2 and (b) NZSP electrolytes. Figure S4: Schematic triangle bottlenecks for Na-Na migration; Figure S5: Ion-migration channels calculated by BVSE for (a) NZSP-2 and (b) pristine NZSP with the channels highlighted by blue shading; Figure S6: Cross-sectional SEM image of pristine NZSP; Figure S7: Cross-sectional SEM–EDS results of pristine NZSP; Figure S8: (a) Cross-sectional SEM image of the NZSP-2 electrolyte after cycling in Na||NZSP-2||Na symmetric cell. (b) Enlarged cross-sectional SEM image selected from (a) and corresponding (c–i) EDS elemental mapping results for Na, Zr, Si, P, Zn, Nb and Hf.

Author Contributions: Y.C.: Conceptualization, Formal analysis, Investigation, Data curation, Writing—original draft. J.W.: Methodology, Investigation, Data curation, Writing—original draft. J.C.: Investigation. Z.H.: Investigation. C.H.: Investigation. F.Q.: Conceptualization, Writing—review and editing, Supervision. Y.Y.: Conceptualization, Writing—review and editing, Supervision, Funding acquisition. All authors have read and agreed to the published version of the manuscript.

Funding: This work was supported by the National Natural Science Foundation of China (No. 12305343).

Data Availability Statement: The data supporting the findings of this study are available from the corresponding author upon reasonable request.

Conflicts of Interest: The authors declare no conflicts of interest.

Appendix A

Table A1. Lattice parameters and refined crystallographic parameters of the $Na_{3.167}Zn_{0.167}Hf_{0.167}Zr_{1.5}Nb_{0.167}Si_2PO_{12}$ (NZSP-2) sample.

Space Group: *C*2/*c* (15); **Lattice Parameters:** ***a* = 15.661 Å, *b* = 9.060 Å, *c* = 9.210 Å, and *β* = 123.857°** ***Z* = 4**					
Label	**Wyckoff**	**Occ.**	**Position**		
			x	***y***	***z***
Na1	4d	1	0.25	0.25	0.5
Zr1	8f	0.75	0.1017 (3)	0.252 (1)	0.0568 (3)
P1	4e	0.333	0	0.042 (3)	0.25
Si1	4e	0.667	0	0.042 (3)	0.25
P2	8f	0.333	0.356 (1)	0.107 (2)	0.262 (2)
Si2	8f	0.667	0.356 (1)	0.107 (2)	0.262 (2)
O1	8f	1	0.157 (2)	0.440 (3)	0.233 (3)
O2	8f	1	0.435 (2)	0.450 (3)	0.073 (3)

Table A1. *Cont.*

Space Group: *C*2/*c* (15); **Lattice Parameters:** ***a* = 15.661 Å, *b* = 9.060 Å, *c* = 9.210 Å, and *β* = 123.857°** ***Z* = 4**					
Label	**Wyckoff**	**Occ.**	**Position**		
			x	***y***	***z***
O3	8f	1	0.254 (2)	0.193 (3)	0.216 (3)
O4	8f	1	0.381 (2)	0.145 (3)	0.129 (3)
O5	8f	1	0.450 (2)	0.184 (3)	0.439 (3)
O6	8f	1	0.073 (2)	0.143 (3)	0.231 (3)
Na2	4e	1	0.5	0.898 (4)	0.25
Na3	8f	0.583	0.830 (3)	0.076 (6)	0.834 (5)
Zn	8f	0.083	0.1017 (3)	0.252 (1)	0.0568 (3)
Hf	8f	0.083	0.1017 (3)	0.252 (1)	0.0568 (3)
Nb	8f	0.083	0.1017 (3)	0.252 (1)	0.0568 (3)

Agreement parameters: R_{wp}% = 10.95 and R_p% = 6.99.

Table A2. Lattice parameters and refined crystallographic parameters of the pristine $Na_3Zr_2Si_2PO_{12}$ sample.

Space Group: *C*2/*c* (15); **Lattice Parameters:** ***a* = 15.660 Å, *b* = 9.060 Å, *c* = 9.205 Å, and *β* = 123.845°** ***Z* = 4**					
Label	**Wyckoff**	**Occ.**	**Position**		
			x	***y***	***z***
Na1	4d	1	0.25	0.25	0.5
Zr1	8f	1	0.1014 (2)	0.2508 (5)	0.0563 (2)
P1	4e	0.333	0	0.035 (2)	0.25
Si1	4e	0.667	0	0.035 (2)	0.25
P2	8f	0.333	0.3566 (6)	0.107 (1)	0.2594 (9)
Si2	8f	0.667	0.3566 (6)	0.107 (1)	0.2594 (9)
O1	8f	1	0.144 (1)	0.432 (2)	0.222 (2)
O2	8f	1	0.432 (1)	0.450 (2)	0.076 (2)
O3	8f	1	0.256 (1)	0.187 (2)	0.216 (2)
O4	8f	1	0.387 (1)	0.147 (2)	0.120 (2)
O5	8f	1	0.454 (1)	0.175 (2)	0.447 (2)
O6	8f	1	0.076 (1)	0.140 (2)	0.233 (2)
Na2	4e	1	0.5	0.895 (2)	0.25
Na3	8f	0.5	0.832 (2)	0.081 (3)	0.848 (3)

Agreement parameters: R_{wp}% = 9.08 and R_p% = 6.63.

Table A3. Critical bond lengths in the refined crystallographic structure of NZSP-2.

Contacts	**Distances (Å)**	**Contacts**	**Distances (Å)**
Na1-O1	2.675 (28)	Si1/P1-O2	1.596 (27)
Na1-O3	2.703 (22)	Si1/P1-O6	1.553 (30)
Na1-O6	2.666 (29)		
		Si2/P2-O1	1.525 (31)
Na2-O1	2.572 (27)	Si2/P2-O3	1.604 (29)
Na2-O4	2.731 (33)	Si2/P2-O4	1.515 (27)
Na2-O5	2.621 (25)	Si2/P2-O5	1.623 (24)

Table A3. *Cont.*

Contacts	Distances (Å)	Contacts	Distances (Å)
Na2-O6	2.62 (4)		
		* M-O1	2.176 (27)
Na3-O1	2.34 (6)	M-O2	2.081 (28)
Na3-O2	2.20 (5)	M-O3	2.055 (25)
Na3-O3	2.68 (5)	M-O4	2.097 (27)
Na3-O6	2.75 (5)	M-O5	2.071 (23)
		M-O6	2.132 (24)

* M denotes Zn, Zr, Hf, or Nb in the M–O bond for NZSP-2.

Table A4. Critical bond lengths in the refined crystallographic structure of NZSP.

Contacts	Distances (Å)	Contacts	Distances (Å)
Na1-O1	2.704 (15)	Si1/P1-O2	1.550 (15)
Na1-O3	2.728 (13)	Si1/P1-O6	1.607 (17)
Na1-O6	2.643 (17)		
		Si2/P2-O1	1.590 (16)
Na2-O1	2.430 (16)	Si2/P2-O3	1.570 (17)
Na2-O4	2.723 (18)	Si2/P2-O4	1.642 (17)
Na2-O5	2.547 (15)	Si2/P2-O5	1.660 (13)
Na2-O6	2.643 (21)		
		Zr-O1	2.084 (15)
Na3-O1	2.503 (30)	Zr-O2	2.082 (16)
Na3-O2	2.146 (28)	Zr-O3	2.098 (14)
Na3-O3	2.699 (32)	Zr-O4	1.960 (15)
Na3-O6	2.793 (27)	Zr-O5	2.048 (14)
		Zr-O6	2.122 (14)

References

1. Hwang, J.Y.; Myung, S.T.; Sun, Y.K. Sodium-ion batteries: Present and future. *Chem. Soc. Rev.* **2017**, *46*, 3529–3614. [CrossRef] [PubMed]
2. Lu, Y.; Li, L.; Zhang, Q.; Niu, Z.; Chen, J. Electrolyte and Interface Engineering for Solid-State Sodium Batteries. *Joule* **2018**, *2*, 1747–1770. [CrossRef]
3. Lee, B.; Paek, E.; Mitlin, D.; Lee, S.W. Sodium Metal Anodes: Emerging Solutions to Dendrite Growth. *Chem. Rev.* **2019**, *119*, 5416–5460. [CrossRef] [PubMed]
4. Gao, W.; Lu, Y.; Tan, X.; Wang, T.; Yu, Y.; Lu, Y.; Zhang, X.; Wang, J.; Liu, Y.; Liu, X.; et al. Sodiophilic design for sodium-metal batteries: Progress and prospects. *Energy Environ. Sci.* **2025**, *18*, 1630–1657. [CrossRef]
5. Wang, X.; Fan, Y.; Li, J.; Li, X.; Li, W.; Wang, J.; Pang, W.K. Comprehensive understanding of the $Na_{1+x}Zr_2Si_xP_{3-x}O_{12}$ solid-state electrolyte in advanced sodium metal batteries: A critical review. *Energy Environ. Sci.* **2025**, *18*, 1096–1129. [CrossRef]
6. Wang, X.; Li, J.; Hu, Z.; Li, X.; Liu, L.; Wang, J.; Kim, J.H.; Li, W.; Pang, W.K.; Johannessen, B. Sc/Mg Co-Doping in $Na_3Zr_2Si_2PO_{12}$ Solid-State Electrolytes Enables Outstanding Performance of Sodium Metal Batteries. *Adv. Sci.* **2025**, *12*, e15463. [CrossRef] [PubMed]
7. Zhang, Z.; Zhang, Q.; Shi, J.; Chu, Y.S.; Yu, X.; Xu, K.; Ge, M.; Yan, H.; Li, W.; Gu, L.; et al. A Self-Forming Composite Electrolyte for Solid-State Sodium Battery with Ultralong Cycle Life. *Adv. Energy Mater.* **2017**, *7*, 1601196. [CrossRef]
8. Goodenough, J.B.; Hong, H.Y.P.; Kafalas, J.A. Fast Na^+-ion transport in skeleton structures. *Mater. Res. Bull.* **1976**, *11*, 203–220. [CrossRef]
9. Hong, H.Y.P. Crystal structures and crystal chemistry in the system $Na_{1+x}Zr_2Si_xP_{3-x}O_{12}$. *Mater. Res. Bull.* **1976**, *11*, 173–182. [CrossRef]
10. Zuo, D.; Tian, J.; Sun, Y.; Yu, X.; Peng, B.; Yu, T.; Xu, C.; Xu, X.; Wang, Y.; Liu, Y.; et al. Machine learning-accelerated discovery of multi-cation entropy-stabilized NASICON solid electrolytes with 10 000 hours of stable Na plating/stripping for all-solid-state sodium batteries. *Energy Environ. Sci.* **2026**, *19*, 860–869. [CrossRef]
11. Zhang, Z.; Zou, Z.; Kaup, K.; Xiao, R.; Shi, S.; Avdeev, M.; Hu, Y.S.; Wang, D.; He, B.; Li, H.; et al. Correlated Migration Invokes Higher Na^+-Ion Conductivity in NaSICON-Type Solid Electrolytes. *Adv. Energy Mater.* **2019**, *9*, 1902373. [CrossRef]

12. He, Y.; Scivally, E.; Shaji, A.; Ouyang, B.; Zeng, Y. Unraveling the Fast Ionic Conduction in NASICON-Type Materials. *Adv. Energy Mater.* **2024**, *15*, 2403877. [CrossRef]
13. Fang, D.; Li, Y.; Wang, C.; Miao, R.; Yang, S.; Zhao, Y.; Ding, Y.; He, J.; Chen, L.; Li, N.; et al. Wide-temperature solid-state sodium metal batteries using Na^+ superionic conductor-type solid electrolytes. *Energy Storage Mater.* **2025**, *74*, 103973. [CrossRef]
14. Luo, M.; Wang, C.; Duan, Y.; Zhao, X.; Wang, J.; Sun, X. Surface Coating Enabling Sulfide Solid Electrolytes with Excellent Air Stability and Lithium Compatibility. *Energy Environ. Mater.* **2024**, *7*, e12753. [CrossRef]
15. Li, R.; Xu, K.; Wen, S.; Tang, X.; Lin, Z.; Guo, X.; Avdeev, M.; Zhang, Z.; Hu, Y.S. A sodium superionic chloride electrolyte driven by paddle wheel mechanism for solid state batteries. *Nat. Commun.* **2025**, *16*, 6633. [CrossRef] [PubMed]
16. Yang, J.; Liu, G.; Avdeev, M.; Wan, H.; Han, F.; Shen, L.; Zou, Z.; Shi, S.; Hu, Y.-S.; Wang, C.; et al. Ultrastable All-Solid-State Sodium Rechargeable Batteries. *ACS Energy Lett.* **2020**, *5*, 2835–2841. [CrossRef]
17. Li, D.; Sun, C.; Wang, C.; Li, J.; Wang, Z.; Jin, H. Regulating Na/NASCION electrolyte interface chemistry for stable solid-state Na metal batteries at room temperature. *Energy Storage Mater.* **2023**, *54*, 403–409. [CrossRef]
18. Samiee, M.; Radhakrishnan, B.; Rice, Z.; Deng, Z.; Meng, Y.S.; Ong, S.P.; Luo, J. Divalent-doped $Na_3Zr_2Si_2PO_{12}$ natrium superionic conductor: Improving the ionic conductivity via simultaneously optimizing the phase and chemistry of the primary and secondary phases. *J. Power Sources* **2017**, *347*, 229–237. [CrossRef]
19. Thirupathi, R.; Omar, S. A Strategic Co-doping Approach Using Sc^{3+} and Ce^{4+} toward Enhanced Conductivity in NASICON-Type $Na_3Zr_2Si_2PO_{12}$. *J. Phys. Chem. C* **2021**, *125*, 27723–27735. [CrossRef]
20. Huang, C.; Yang, G.; Yu, W.; Xue, C.; Zhai, Y.; Tang, W.; Hu, N.; Wen, Z.; Lu, L.; Song, S. Gallium-substituted Nasicon $Na_3Zr_2Si_2PO_{12}$ solid electrolytes. *J. Alloys Compd.* **2021**, *855*, 157501. [CrossRef]
21. Wang, Q.; Yu, C.; Li, L.; Liu, X.; Zhang, X.; Gao, G.; Wang, Y.; Li, G. Sc-doping in $Na_3Zr_2Si_2PO_{12}$ electrolytes enables preeminent performance of solid-state sodium batteries in a wide temperature range. *Energy Storage Mater.* **2023**, *54*, 135–145. [CrossRef]
22. Luo, Y.; Fang, X.; Xiao, J.; Huang, Z.; Xiong, J.; Jiang, G.; Yuan, S. Optimizing the Na/NASCION electrolyte interface for stable solid-state Na metal batteries. *J. Alloys Compd.* **2024**, *991*, 174529. [CrossRef]
23. Li, Z.; Zhang, M.; Yan, Y.; Zhang, W.; Meng, X.; Yang, N. Sc/Zn co-doped NASICON electrolyte with high ionic conductivity for stable solid-state sodium batteries. *EES Batter.* **2025**, *1*, 1740–1750. [CrossRef]
24. Cheung, E.A.; Nguyen, H.; Avdeev, M.; de Souza, N.R.; Meng, Y.S.; Sharma, N. Insights into the Fast Sodium Conductor NASICON and the Effects of Mg^{2+} Doping on Na^+ Conductivity. *Chem. Mater.* **2021**, *33*, 8768–8774. [CrossRef]
25. Shannon, R.D. Revised effective ionic radii and systematic studies of interatomic distances in halides and chalcogenides. *Acta Crystallogr. Sect. A* **1976**, *32*, 751–767. [CrossRef]
26. Zeng, Y.; Ouyang, B.; Liu, J.; Byeon, Y.W.; Cai, Z.; Miara, L.J.; Wang, Y.; Ceder, G. High-entropy mechanism to boost ionic conductivity. *Science* **2022**, *378*, 1320–1324. [CrossRef] [PubMed]
27. Chen, H.; Wong, L.L.; Adams, S. SoftBV—A software tool for screening the materials genome of inorganic fast ion conductors. *Acta Crystallogr. B Struct. Sci. Cryst. Eng. Mater.* **2019**, *75*, 18–33. [CrossRef] [PubMed]
28. He, K.Q.; Liao, X.G.; Lian, H.J.; Guan, X.; Chen, D.Z.; Su, Y.K.; Li, R.K.Y.; Liu, C. Endowing rapid Na^+ conduction by architecture design of $Na_3Zr_2Si_2PO_{12}$ in composite electrolytes for ultralong lifespan quasi-solid-state sodium metal batteries. *Rare Met.* **2025**, *44*, 3795–3805. [CrossRef]
29. Yu, X.; Yao, Y.; Wang, X.; Cen, S.; Li, D.; Ma, H.; Chen, J.; Wang, D.; Mao, Z.; Dong, C. Rapid ultrasound welding toward compact Na/Beta-Al_2O_3 interface realizing room-temperature solid-state sodium metal battery. *Energy Storage Mater.* **2023**, *54*, 221–226. [CrossRef]
30. Li, D.; Wang, X.; Guo, Q.; Yu, X.; Cen, S.; Ma, H.; Chen, J.; Wang, D.; Mao, Z.; Dong, C. Atomically bonding Na anodes with metallized ceramic electrolytes by ultrasound welding for high-energy/power solid-state sodium metal batteries. *Carbon Energy* **2023**, *5*, e299. [CrossRef]
31. Wang, X.; Yu, X.; Wang, X.; Chen, J.; Wang, D.; Dong, C.; Mao, Z. Reinforced Li/Garnet Interface by Ceramic Metallization-Assisted Room-Temperature Ultrasound Welding. *Carbon Neutraliz.* **2025**, *4*, e185. [CrossRef]
32. Wang, Q.; Jiang, Z.; Yu, C.; Li, L.; Li, G. Research progress of inorganic sodium ion conductors for solid-state batteries. *Chin. Chem. Lett.* **2025**, *36*, 110006. [CrossRef]

Disclaimer/Publisher's Note: The statements, opinions and data contained in all publications are solely those of the individual author(s) and contributor(s) and not of MDPI and/or the editor(s). MDPI and/or the editor(s) disclaim responsibility for any injury to people or property resulting from any ideas, methods, instructions or products referred to in the content.